Volume 17 | Number 30 | 14 August 2015 | Pages 5581–5862

CrystEngComm

www.rsc.org/crystengcomm

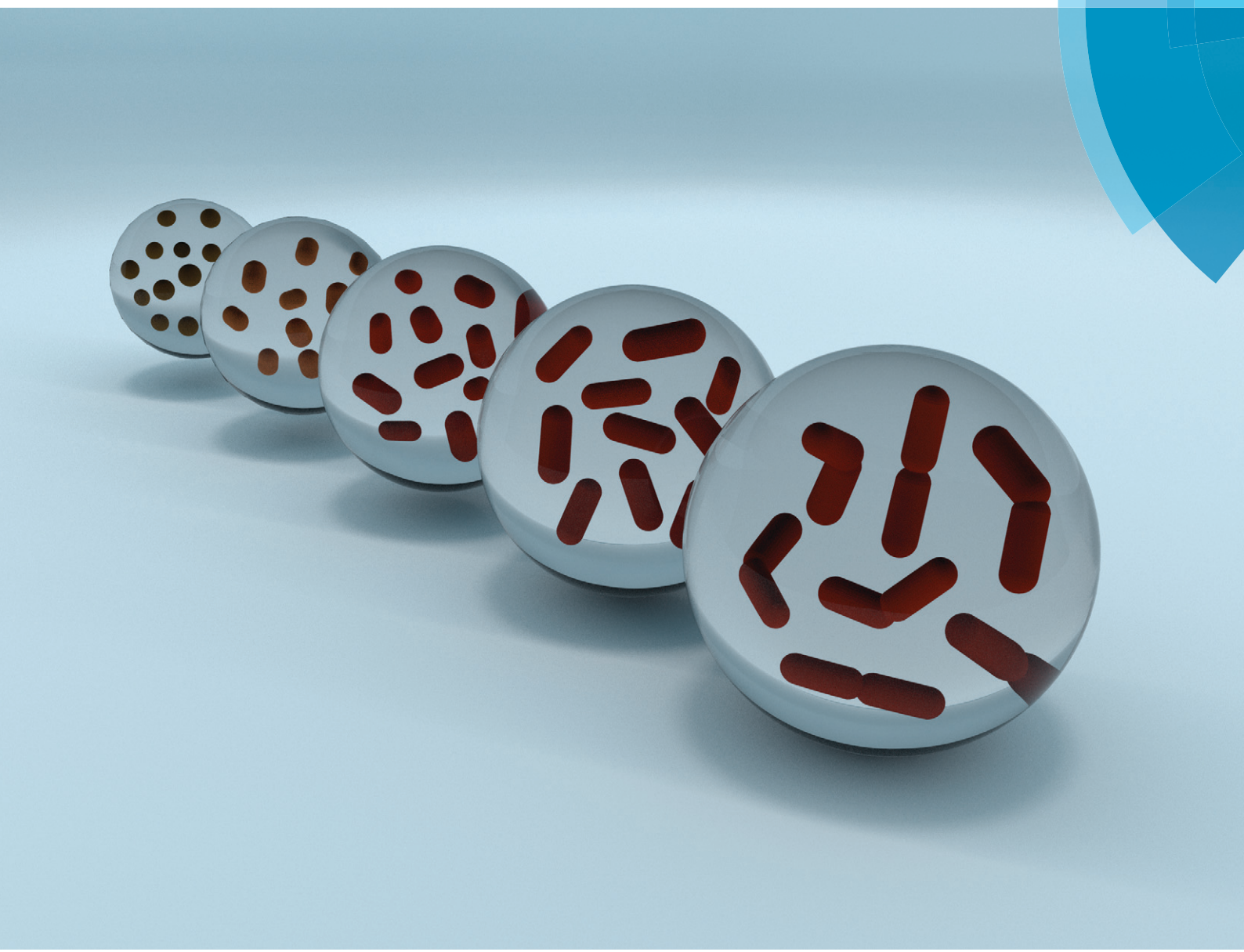

ROYAL SOCIETY OF CHEMISTRY

PAPER

Joanna Kolny-Olesiak *et al.*

Alloyed $CuInS_2$–ZnS nanorods: synthesis, structure and optical properties

CrystEngComm

PAPER

View Article Online
View Journal | View Issue

Cite this: *CrystEngComm*, 2015, **17**, 5634

Alloyed $CuInS_2$–ZnS nanorods: synthesis, structure and optical properties†

Jie Li,[a] Björn Kempken,[a] Volodymyr Dzhagan,[bc] Dietrich R. T. Zahn,[b] Justyna Grzelak,[d] Sebastian Mackowski,[de] Jürgen Parisi[a] and Joanna Kolny-Olesiak*[a]

Received 24th February 2015,
Accepted 28th April 2015

DOI: 10.1039/c5ce00380f

www.rsc.org/crystengcomm

Alloyed $CuInS_2$–ZnS nanocrystals are promising candidates for application in biolabeling, photocatalysis, solar energy conversion, and light emitting diodes. When charge transport is of importance, elongated nanoparticles are advantageous, because of their higher electrical conductivity compared to the quasi-spherical ones. However, still little is known about the growth mechanism of such nanostructures composed of quaternary materials. Here, $CuInS_2$–ZnS nanorods were synthesized by a heating-up method, and their Zn content was controlled by changing the composition of the reaction solution. A mixture of oleylamine and oleic acid is used as solvent. Copper, indium, and zinc acetate are the sources of the cations, while sulfur monomers stem from the thermal decomposition of *tert*-dodecanethiol. The growth of $CuInS_2$–ZnS nanorods starts with the formation of copper sulfide particles. They are gradually converted to $CuInS_2$–ZnS by incorporation of indium and zinc ions. Alloyed $CuInS_2$–ZnS nanorods are the only product, independent of the amount of zinc applied; Raman spectroscopy measurements show no separate ZnS phase. At longer reaction time, the nanorods aggregate to form dimers. The onset of the absorption and the position of the maximum of the emission as well as the fluorescence lifetime depend on the composition of the nanorods.

Introduction

Semiconductor nanocrystals attract scientific attention due to their size and shape dependent properties. However, most of the best-studied materials contain toxic elements, such as cadmium or lead, which severely restricts their application potential. One of the possible alternatives, which does not involve highly toxic heavy metals, is $CuInS_2$ (CIS),[1–3] a direct semiconductor (bandgap of the bulk, 1.55 eV; Bohr exciton radius, 4 nm)[4] with a high absorption coefficient (~10^5 cm^{-1} at 500 nm),[5] photostability, and biocompatibility. The emission of $CuInS_2$ nanocrystals can be tuned between 950 nm and 500 nm by decreasing the size of the crystallites. However, small particles are less stable and have lower quantum yields than the larger ones. Another approach to change the optical properties uses alloying of $CuInS_2$ with ZnS. $CuInS_2$ and ZnS have similar crystallographic structures, and the lattice mismatch between the two materials is only 2.2%; therefore, copper and indium ions can be easily replaced by zinc ions, and homogeneous alloys can be produced within the whole composition range (between 0% and 100% ZnS). The bandgap of ZnS–$CuInS_2$ alloys (ZCIS) can vary between 1.55 and 3.7 eV (bandgaps of bulk CIS and ZnS, respectively), while the positions of the HOMO and the LUMO should lie between those of pure $CuInS_2$ and ZnS. Density functional theory calculations[6] show that the valence band of ZCIS is formed from Cu 3d and S 3p orbitals, while the In 5s5p and Zn 4s4p orbitals contribute to the formation of the conduction band. Thus, only by varying the ZnS content in the alloy can the position of the energy levels be influenced, and we end up with nanocrystals with absorption covering the whole visible spectrum. This makes ZCIS nanoparticles (NPs) promising for applications in biolabelling,[7–9] photocatalysis,[10,11] solar energy conversion,[12,13] and light emitting diodes.[14–17]

Such application potential motivates materials scientists to develop methods to synthesize uniform defect-free ZCIS crystallites with a defined size, shape, and composition. The challenge in the synthesis of this quaternary compound is adjusting the reactivity of three cationic precursors with different chemical properties. The latter can be done by the

[a] *Energy and Semiconductor Research Laboratory, Department of Physics, Carl von Ossietzky University of Oldenburg, 26129 Oldenburg, Germany. E-mail: joanna.kolny@uni-oldenburg.de*
[b] *Semiconductor Physics, Technische Universität Chemnitz, 09107 Chemnitz, Germany*
[c] *V.E. Lashkaryov Institute of Semiconductor Physics, National Academy of Science of Ukraine, Kyiv 03028, Ukraine*
[d] *Optics of Hybrid Nanostructures Group, Faculty of Physics, Astronomy and Informatics, Nicolaus Copernicus University, Torun, Poland*
[e] *Nanotechnology Department, Wroclaw Research Centre EIT+, Stablowicka 147, 54-066 Wrocław, Poland*

† Electronic supplementary information (ESI) available: Original Raman spectra of the nanorod samples, Tauc plots and fluorescence decay curves, the corresponding fits, and the resulting decay constants. See DOI: 10.1039/c5ce00380f

right choice of ligands and reaction conditions. Several examples of a direct synthesis of ZCIS NPs were described in the literature recently;[11,18–21] *e.g.*, Pan *et al.*[20] applied thermolysis of complexes of dithiocarbamate with Zn^{2+}, Cu^{2+}, and In^{3+} in the presence of oleylamine as an activating agent, which facilitated the formation of homogeneous nanocrystals. Another approach is a two-step procedure, in which $CuInS_2$ crystallites are synthesized first, and alloy particles are obtained by cation exchange.[11,22] Some of these methods allow for a precise control of the composition, and, consequently, of the optical properties of quasi-spherical[19,20] or cube-shaped[9] alloyed nanocrystals; however, no formation of anisotropic shapes was reported. Growth of elongated structures can be obtained by a two-step method, using copper sulfide particles as seeds for the growth of another semiconductor material ($CuInS_2$,[23–25] ZnS,[25] or $CuInS_2$–ZnS[23,25]).[26] Thus, uniform alloyed ZCIS nanorods were obtained as part of a heterostructure, containing also copper sulfide.[23,25] However, the emission properties of this material have not been reported, and the growth process of the nanorods has not been investigated in detail, yet.

In the present work, we introduce a heating-up synthesis of ZCIS nanorods. Our procedure is based on the synthesis of $CuInS_2$ nanorods and nano-networks we developed recently.[27] It can be easily scaled up, which is particularly important in view of future applications of the present material class. By changing the amount of Zn ions applied, we can vary the composition of the nanorods and their optical properties. The nanorods were characterized by transmission electron microscopy (TEM), X-ray diffraction (XRD), Raman scattering, UV–vis absorption, as well as steady-state and time-resolved emission spectroscopy.

Experimental

Chemicals

Copper(I) acetate (CuAc, 97%), zinc acetate (ZnAc, 99.99%), 1-dodecanethiol (1-DDT, 98%), *tert*-dodecanethiol (*t*-DDT, 98.5%), and oleic acid (OA, 90%) were purchased from Aldrich. Oleylamine (OLAM, 80–90%) and indium(III) acetate ($InAc_3$, 99.99%) were delivered from Acros and Alfa Aesar, respectively. All chemicals were used without further purification.

Synthesis of ZCIS alloy nanorods

In a typical heating-up procedure, all materials were mixed together in a three-neck flask, including 0.5, 1.0, 1.5, or 2.0 mmol zinc acetate (samples ZnS : CIS 1 : 2, ZnS : CIS 1 : 1, ZnS : CIS 3 : 2, and ZnS : CIS 2 : 1, respectively; the numbers denominate the ratio between the Zn^{2+} and the In^{3+} ions in the reaction solution), 1.5 mmol copper acetate, 1 mmol indium acetate, 16 mL (50 mmol) of OA, 10 mL of oleylamine, 0.25 mL of 1-dodecanethiol (1-DDT), and 2.5 mL of *tert*-dodecanethiol (*t*-DDT). After 30 minutes of stirring under vacuum at room temperature, a turbid blue green solution was obtained. The reaction system was subsequently heated to 200 °C under nitrogen flow. Small aliquots were taken out during different time intervals between 30 s and 1 h. Finally, the reaction system was cooled to room temperature, and the ZCIS nanoparticles obtained were precipitated and washed by adding ethanol to remove residual thiols, acetates, and OA. The purified precipitate was then redissolved in hexane.

Characterization

UV–vis and PL spectra were obtained using a Varian Cary 50 Scan spectrophotometer and a Fluorolog Jobin Yvon spectrofluorometer, respectively. Fluorescence decays were measured for solutions of the nanorods using time-correlated single photon counting. As the excitation source, a DPSS laser was used, which provided 30 ps pulses with a 20 MHz repetition rate at the wavelength of 405 nm. TEM images were acquired using a Zeiss EM 902A transmission electron microscope with an acceleration voltage of 80 kV. Powder X-ray diffraction was obtained by wide-angle X-ray scattering using a PANalytical X'Pert PRO MPD diffractometer equipped with Cu Ka radiation. Rietveld refinement was conducted using the program MAUD v. 2.33. Texture effects were studied using the harmonic texture model implemented into the MAUD program. The anisotropy of the shape of the particles was analyzed using a size-strain model developed by Popa.[28] The samples were measured on low background silicon sample holders. The integral stoichiometry was obtained by the EDAX detector integrated into a FEI Quanta 200 3D scanning electron microscope. Raman scattering spectra were excited with the 633 nm lines of an He–Ne laser and registered with a HR LabRam spectrometer and a spectral resolution of 2 cm^{-1}. The incident laser power was kept below 0.02 mW, in order to avoid sample heating under the microscope objective (50×).

Results and discussion

ZCIS nanorods were synthesized in a mixture of oleic acid (OA) and oleylamine (OLAM) as solvent, using copper, indium, and zinc acetate as cationic precursors. *tert*-Dodecanethiol (*t*-DDT) served as the main sulfur source, because it can be easily decomposed thermally.[23,29–31] 1-DDT (thermally more stable, compared to *t*-DDT) and OA acted as stabilizers. All the educts were mixed together at room temperature and then heated to the reaction temperature. The results of such a heat-up synthesis do not significantly differ from a hot-injection reaction with the same educts. However, the benefit of the heat-up method is its potential for up-scaling, without losing the quality (*e.g.*, the narrow size distribution) of the NPs, which is of advantage for future application of these particles.

The Results and discussion section is organized in the following manner: we describe first the morphology, crystallographic structure, and composition of the nanorods synthesized with different zinc fractions in the reaction solution, based on TEM, XRD, and Raman spectroscopy results. The next section is devoted to the optical properties of these

particles obtained by UV–vis absorption as well as steady-state and time-resolved emission spectroscopy. The last part of the manuscript describes the details of the growth process of the nanorods.

Morphology, structure, and composition

Fig. 1 shows the TEM images of nanorods with different amounts of Zn. Elongated ZCIS alloy nanocrystals were obtained independent of the concentration of Zn ions used in the reaction. Some differences in the morphology of the final particles were, however, observed. Even though all particles shown in Fig. 1 were synthesized under identical reaction conditions (time, temperature), the length of the nanorods ranges from ~10 to ~20 nm. The uniform, short nanorods in sample ZnS : CIS 1 : 2 exhibit a pronounced tendency towards self-organization perpendicular to the substrate, as can be seen in Fig. 1a. Particles synthesized with higher zinc contents of the reaction solution are longer (Fig. 1b, c, and d); furthermore, aggregation of primary nanorods to dimers with a linear or bipod geometry could be observed in the sample ZnS : CIS 1 : 1 (Fig. 1b, 2b and c). In contrast to our previous results with pure $CuInS_2$,[27] we do not observe preferential formation of tetrapods or larger networks here. High-resolution TEM (HRTEM) images show that the nanorods are single crystalline (Fig. 2a), while the dimers are composed of two crystalline domains. This observation is also supported by the XRD analysis of these samples, presented in the section describing the growth process of the nanorods.

The X-ray diffraction measurements reveal that the nanorods have a wurtzite structure (Fig. 3). The lattice parameters

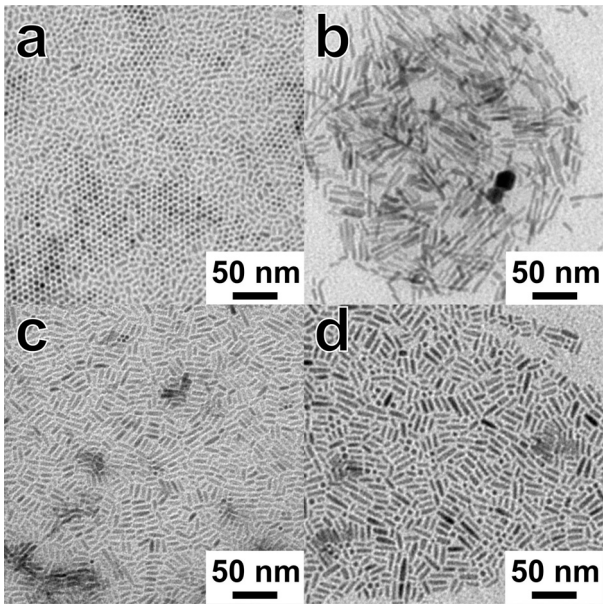

Fig. 1 Overview of the TEM images of samples ZnS : CIS 1 : 2 (a), ZnS : CIS 1 : 1 (b), ZnS : CIS 3 : 2 (c), and ZnS : CIS 2 : 1 (d). Particles with circular projection in panel (a) are nanorods oriented with their long axis perpendicular to the substrate.

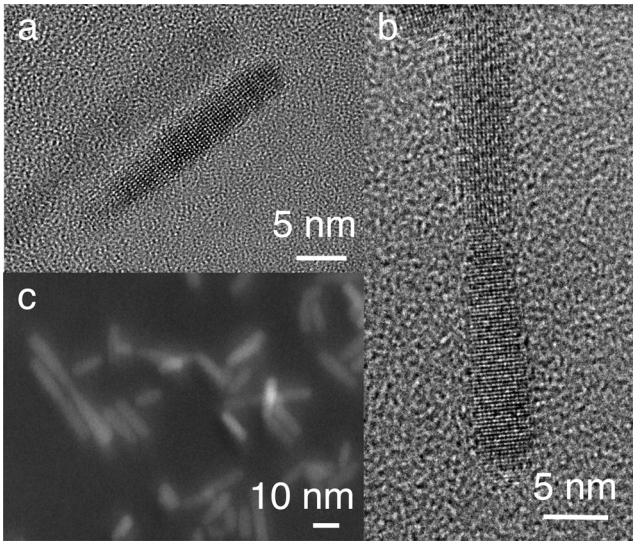

Fig. 2 HRTEM image of a single nanorod (a), a linear dimer of nanorods (b), and a dark field image obtained with a high angle angular detector, showing both nanorods and dimers (c).

of the alloyed nanorods lie between that of pure CIS and ZnS (see Table 1), which confirms the alloy formation. The shape models obtained from Rietveld refinement (inset in Fig. 3) show that the particles grow along the *c*-axis of the wurtzite structure. The aspect ratio of the nanorods is between 1.9 and 3.4 (Table 1). The broadening of the reflections in the XRD pattern not only is due to the small size of the crystallites, but also originates from strain. The results of the Rietveld refinement show *hkl*-dependent values of strain (for the values obtained for the 100 and 002 reflections, see Table 1). Uniform strain would cause an isotropic expansion or contraction of the unit cell and would not result in broadening of the reflections. Peak broadening originates from shifts of atoms from their ideal positions, induced by anisotropic strain arising from lattice defects. Also variations in

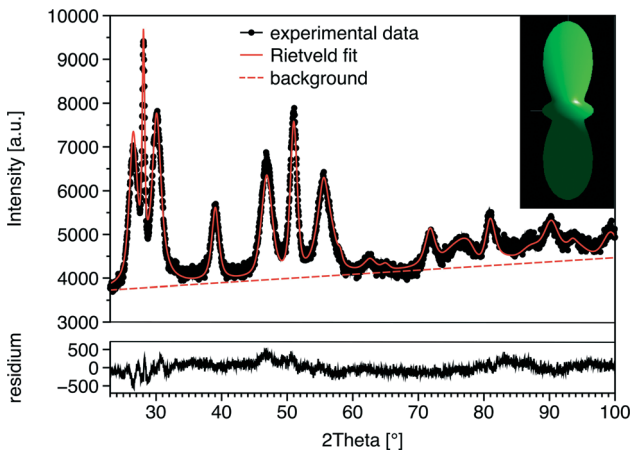

Fig. 3 XRD pattern and results of Rietveld refinement of the sample ZnS : CIS 3 : 2. The inset shows the shape model obtained from the Rietveld analysis.

Table 1 Results of Rietveld refinement of samples with different Zn contents

	ZnS : CIS 1 : 2	ZnS : CIS 1 : 1	ZnS : CIS 3 : 2	ZnS : CIS 2 : 1
Unit cell parameter a [Å]	3.8886 ± 0.00039	3.8900 ± 0.00037	3.8739 ± 0.00016	3.8667 ± 0.00015
Unit cell parameter c [Å]	6.4109 ± 0.00095	6.3806 ± 0.00071	6.3489 ± 0.00018	6.3542 ± 0.0028
Size $\perp c$ axis [nm]	7.0	7.2	6.4	5.9
Size $\|\|c$ axis [nm]	13.3	16.4	21.4	13.6
Aspect ratio	1.9	2.3	3.4	2.3
Strain $\perp c$ axis [%]	1.26	1.33	1.06	1.06
Strain $\|\|c$ axis [%]	0.45	0.24	0.24	0.28

the exact composition between the particles can be a reason for this kind of strain-like broadening of the reflections. For the quaternary particles studied here, both defects and fluctuations in composition are a likely explanation for the strain values observed.

The composition of the samples obtained from reactions with different Zn contents was studied by energy dispersive X-ray spectroscopy (EDX). The ratio between the copper and indium ions is 1 : 1 for all four samples. Furthermore, we observe linear dependence of the molar fraction of ZnS within the alloy and the amount of Zn applied in the synthesis (blue squares in Fig. 4). However, the slope of this curve is lower than 1, indicating that some amount of the Zn ions remains in the reaction solution after the synthesis. We also calculated the composition of the samples based on the changes of the lattice parameters, induced by the incorporation of Zn ions into the wurtzite structure of $CuInS_2$. The lattice parameters of different samples were obtained by Rietveld analysis (see above). We assumed linear dependence of the lattice parameters from the composition (Vegard's law) and calculated the fraction of ZnS within the alloy from the changes of the c axis. The resulting values for the Zn content in the nanorods also show approximately linear dependence on the amount of the Zn ions in the reaction solution. However, the values obtained from XRD analysis are lower than those from EDX. It is worth noting that the absolute values obtained from the above calculation strongly depend on the lattice parameters used for pure ZnS and CIS. While reference data for bulk wurtzite ZnS can be found in databases, and its structure has been thoroughly studied, not much information exists about CIS with a wurtzite structure. This polymorph of CIS is stable in the temperature range 1045 and 1090 °C (melting point of CIS). Nanocrystalline CIS with a wurtzite structure was synthesized in 2008 by Pan *et al.*,[32] who estimated the lattice parameters to be $a = b = 3.897(3)$ Å, $c = 6.441(0)$ Å. However, judging from the broadening of the reflections of the XRD patterns presented in this work, these lattice parameters were obtained for a relatively small size of the crystallites. Therefore, they can differ from that of the bulk material; size dependent changes of the lattice parameters were described previously, *e.g.*, for CdTe, PbS, CeO_2, or Sn.[33–36] Larger CIS particles with a wurtzite structure were synthesized by Kruszynska *et al.*[23,30] For our calculation of the ZnS content of the nanorods, we used the values from ref. 23, which were obtained from Rietveld refinement of XRD data of nanorods with a width of 21 nm and a length of 56 nm ($a = b = 3.9062(2)$ Å and $c = 6.4251(10)$ Å).

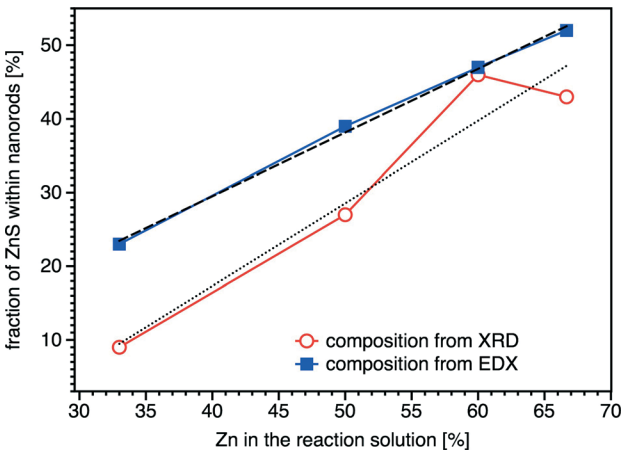

Fig. 4 ZnS content in nanorods synthesized with different amounts of Zn in the reaction solution obtained from EDX measurements and from evaluation of the changes of the lattice parameters, plotted against the zinc content of the reaction solution.

Another explanation of the discrepancy between the values obtained from EDX and XRD data could be the formation of a core–shell structure with a core consisting of a ZCIS alloy and thin ZnS shell. However, the presence of the ZnS phase in nanorods is not supported by the results of Raman scattering on phonons (Fig. 5), as discussed in the following paragraphs.

Fig. 5a shows the Raman scattering spectra of ZCIS nanorods with different ZnS contents. The photoluminescence (PL) background was subtracted, and the curves were normalized with respect to the main peak intensity, in order to improve the visibility of the spectral changes induced by variation of the Zn content. The general appearance of all spectra is similar to the spectrum of pristine CIS NPs with a wurtzite structure reported earlier.[37] Particularly, the group of first-order scattering features in the frequency range of ν ~ 200–400 cm^{-1} is followed by second-order (ν < ~500–700 cm^{-1}) and third-order (ν < ~1000 cm^{-1}) bands (Fig. 5a). Only for the nanorods with the highest Zn content (ZnS : CIS 2 : 1) could no higher order scattering be discerned, because of the huge PL background (see the original Raman spectra in Fig. S1†). The Raman features broaden and shift continuously upward with the increasing Zn content, as can be

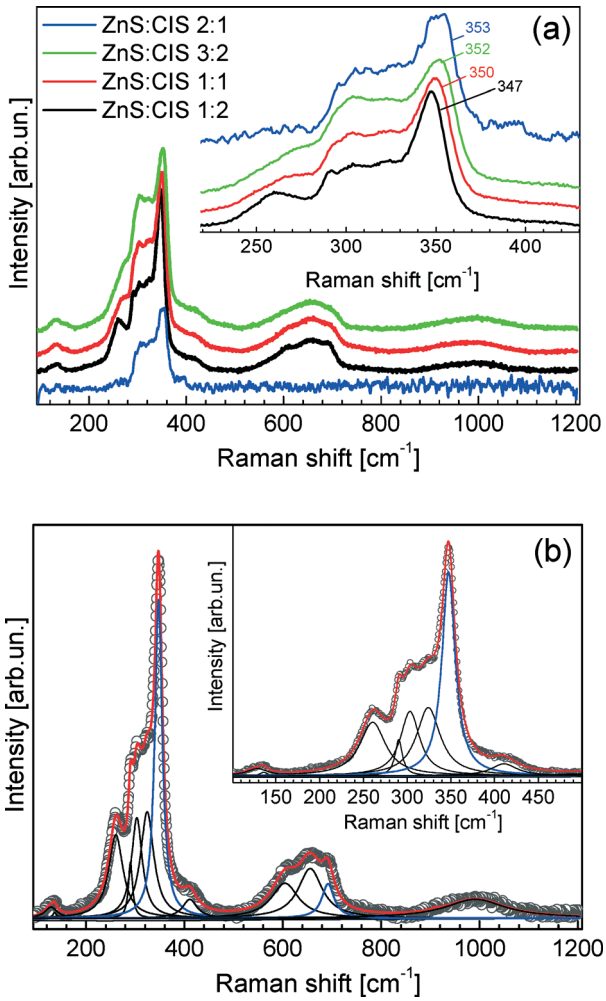

Fig. 5 (a) Normalized Raman spectra of ZCIS nanorods with different ZnS contents (λ_{exc} = 633 nm). Spectra are normalized to the strongest peak intensity, at 350 cm^{-1}. Spectrum of the sample ZnS : CIS 2 : 1 is normalized to a lower intensity, in order to provide better visibility of the spectral changes in other spectra. The inset shows the first-order vibration region in more detail, with the maximum position of the strongest peak indicated for each sample. (b) Fitting of the Raman spectrum of the sample with the lowest Zn content.

seen from the inset in Fig. 5a, where the spectral region of the first-order phonons is shown in more detail. The upward shift of the spectrum between the lowest and the highest Zn content is about 5 cm^{-1}, as measured for the best resolved feature near 350 cm^{-1} (Fig. 5a). The only vibrational peaks for which this trend is not obvious are those below 150 cm^{-1}.

It should be noted that the phonon spectrum of the ZCIS heterosystem has not been studied in detail up to now. The authors of ref. 38 observed a strong enhancement of the vibrational modes at 260 and 343 cm^{-1} upon doping a CIS film with Zn and assigned them to intrinsic cation–anion vibrations of the CIS lattice. In contrast to this, the Raman peak at 353 cm^{-1} found in ZCIS NPs by the authors of ref. 39 was assigned to the ZnS phase and found to be in agreement with their XRD data.

Broadening of the phonon peaks of the CIS lattice by introducing more Zn atoms into it, which is observed in our work, is in accordance with the common behaviour of phonons in alloys.[40,41] The anisotropy of an intrinsic strain, detected from broadening of the XRD reflections, cannot fully account for the Raman peak width. This value, taken as the difference between the strains parallel and perpendicular to the *c*-axis (Table 1), does not change with the Zn content and is equal to 0.8%, while the Raman width slightly increases with the Zn content (Fig. 5). The upward shift of the phonon frequencies can also be explained by the increasing concentration of the Zn atoms embedded into the CIS lattice. Such an increase in the vibrational frequency, dependent on the Zn content, was already observed in $Cd_{1-x}Zn_xS$ and $Cu_2(Zn_xFe_{1-x})SnS_4$ alloys.[40,41]

The growth of the ZCIS nanorods with a high ZnS content might be accompanied by the generation of separate ZnS NPs or the formation of a ZnS shell on the surface of the ZCIS nanorods. We have to consider such a possibility, because the strongest phonon peak at around 350 cm^{-1} wavelength observed in the Raman spectra of our nanorods coincides with the frequency of the longitudinal optical (LO) phonon of ZnS and ZnS based alloys.[40] However, two facts disprove the ZnS phase formation in our case. We do not observe a correlation of the relative intensity of the 350 cm^{-1} peak (with respect to other features in the spectrum) with the Zn content. Furthermore, an inherent vibration of an alloy can be distinguished from that in a pure ZnS crystallite by changing λ_{exc} from a value resonant for the ZCIS alloy (633 nm in our case) to the one resonant for the tentative ZnS crystallites/shells (λ_{exc} = 325 nm).[42] For example, this approach was successfully employed for identification of ZnS as a secondary phase in Cu_2ZnSnS_4.[42,43] In our samples, we registered no Raman peaks when using λ_{exc} = 325 nm (spectra not shown). Therefore, the peak observed at around 350 cm^{-1} at λ_{exc} = 633 nm (Fig. 5) is related to the vibrations in the alloyed rods, with no (or too thin to be detectable) pure ZnS shell being formed. Note that previous studies on colloidal II–VI NPs showed that (non-alloyed) ZnS shells as thin as ~1–2 nm can be detected by resonant Raman spectroscopy, based on the evolvement of intrinsic shell phonons.[44] Besides introducing an own mode to the Raman spectrum, the shell could reduce the peak width of the phonons of the core. For II–VI core/shell NPs, this reduction can reach up to 50% of the peak width.[44] Our ZCIS nanorods show slight, continuous broadening of the Raman peaks with the increasing Zn content instead (Fig. 1a), *i.e.*, a typical behaviour of a phonon in an alloy.

Optical properties

The absorption spectra of the nanorods with different Zn contents show a blue shift compared to the absorption of pure CIS (Fig. 6). The diameter of the nanorods is about the same for all samples, irrespective of their composition, and it is approximately equal to the Bohr exciton diameter of pure

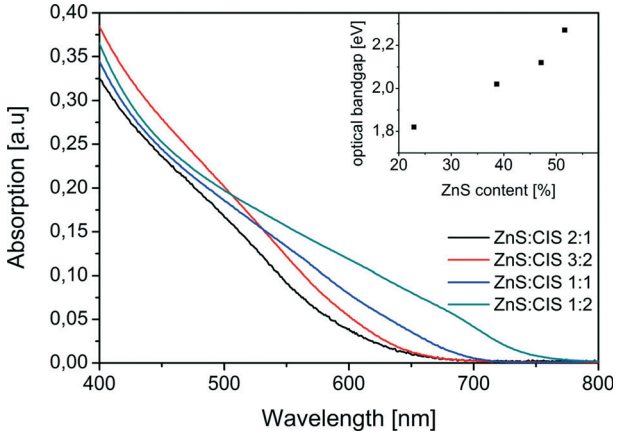

Fig. 6 Absorption spectra of ZCIS nanorods with different ZnS contents. The inset shows the optical bandgap obtained from the Tauc plots shown in Fig. S2 of the ESI.†

CIS (8 nm) and larger than that of ZnS (5 nm). Therefore, we conclude that the changes in the absorption stem mainly from the different compositions of the samples, while the size effects play a minor role. The value of the blue shift depends on the percentage of Zn ions incorporated into the CIS lattice. The optical bandgap of the particles, which was determined from Tauc plots[45] (see Fig. S2 in the ESI†), varies from 1.82 eV for the sample ZnS : CIS 1 : 2 to 2.27 eV for ZnS : CIS 2 : 1. The linear relationship of absorbance squared *versus* energy (see Fig. S2†), found for all four spectra, corresponds to a direct transition. The dependence of the optical bandgap on the composition of the nanorods has a non-linear behaviour with the slope increasing for larger ZnS contents (see the inset in Fig. 6). This is in agreement with the results reported by Pan *et al.*[20] for quasi-spherical ZCIS nanocrystals with varying compositions.

Also the wavelength of the photoluminescence (PL) of the samples depends on the Zn content. In Fig. 7, we show normalized PL spectra obtained for the samples with an increased Zn content. The excitation wavelength of 450 nm was used. Upon increasing the Zn content in the nanorods, the maximum of the emission shifts towards higher values of the energy, which is in accordance with the expected bandgap dependence and UV–vis spectra presented in Fig. 6. However, as can be seen in Fig. 7, the shape of the spectrum changes qualitatively for the sample with the highest Zn content. While for the other samples the spectra feature the most intense red-emitting band accompanied by a wing on its higher value of the quantum energy, in the case of the sample with the highest Zn content, the situation reverses. The latter change is also reflected in the fluorescence excitation spectra, as shown in Fig. 8: the sample with the highest Zn content is characterized by a sharp resonance at 370 nm (Fig. 8b), while all the remaining nanorods exhibit broad excitation spectra, typical for colloidally synthesized semiconductor NPs (Fig. 8a). We note that the qualitative character of the emission spectra is independent of the excitation wavelength in the range from 400 to 480 nm, *i.e.*, in the range where all samples can be excited.

Complementary results obtained for pulsed picosecond excitation are displayed in Fig. 9, where normalized fluorescence decay curves are present. In this case, the excitation wavelength was set to 405 nm. While in the case of the samples with three lower Zn contents, we again observe a monotonic behaviour of the fluorescence decay, namely, the

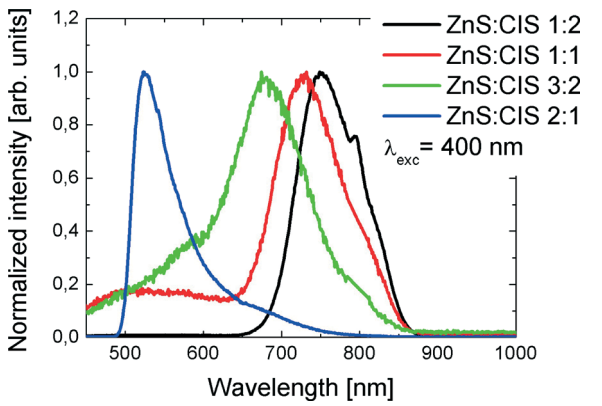

Fig. 7 PL spectra of ZCIS nanorods with different ZnS contents (λ_{exc} = 450 nm).

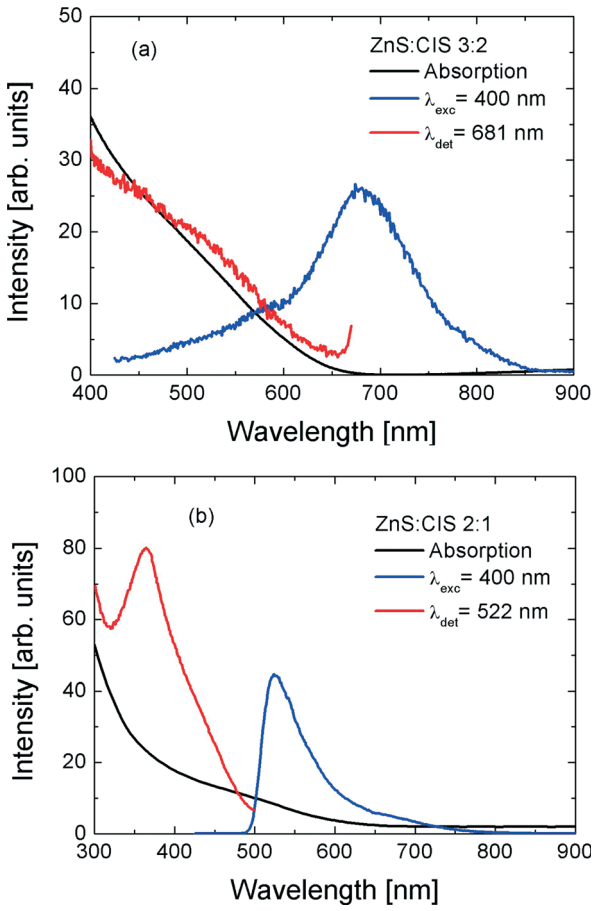

Fig. 8 Comparison of absorption (black), photoluminescence (red), and photoluminescence excitation (blue) spectra of (a) ZnS : CIS 3 : 2 and (b) ZnS : CIS 2 : 1.

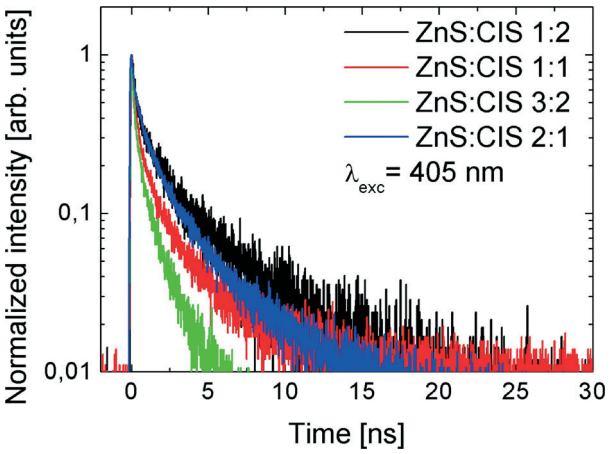

Fig. 9 Fluorescence decay time curves measured with λ_{exc} = 405 nm for the samples with varied Zn contents.

lifetime gets shorter with the increasing content of Zn in the nanorods, and the sample ZnS : CIS 2 : 1 exhibits a longer decay time. The transients can be approximated with a three-decay behaviour; the examples of fits and the resulting decay constants are listed in the ESI† (Fig. S2 and Table S1).

For CIS and ZCIS NPs the typical lifetimes are in the range of hundreds of nanoseconds;[46] however, some authors report also short time components, <10 ns.[4] A similar large spread of lifetimes can be deduced from existing data on Cu–In–S–Zn[47] and related NP systems, like Ag–In–S–Zn.[48] Even the reports on the effect of Zn introduction into CIS NCs are not univocal. Thus in ref. 22 the presence of Zn did not change the lifetime significantly and the observed change of ~10% can be easily caused by other factors, such as the composition of the ligand shell. In contrast, in ref. 49 the contributions of short- and long-lifetime components differ significantly for CIS and ZCIS NPs. Thus the PL lifetime seems to be determined by the defect structure and the coupling to the environment (*e.g.*, ligands) rather than the morphology of the NP.

The correlation between PL and photoluminescence excitation (PLE) spectra of the sample ZnS : CIS 2 : 1 might suggest the presence of ZnS inclusions/shells in this sample. However, in both cases of quasi-0D inclusions and quasi-2D shells, their absorption edge would be significantly blue shifted from the bulk position due to the quantum confinement effect. Instead, the PLE feature of sample ZnS : CIS 2 : 1 occurs at 3.35 eV (370 nm), which is significantly lower than the bandgap of bulk ZnS, ~3.65 eV (340 nm). Therefore, the distinct PLE and PL features of the sample ZnS : CIS 2 : 1 do not originate from the pure ZnS phase in this sample, which is in agreement with the results of Raman spectroscopy. The observed behaviour of the PL and PLE spectra at the highest Zn content can probably be explained with the formation of sub-ensembles of nanorods or parts of each nanorod with noticeably different Zn contents (stoichiometry), in particular, nanorods with a Zn-rich surface. Further investigations on the single-particle level are to be undertaken in order to establish whether the potential compositional inhomogeneity stems from different NPs or from different parts of the same NP. Besides the EDX, which is capable of probing the chemical composition of single NPs, single-nanoparticle PL spectroscopy is planned to be used for solving the above ambiguity in our PL and PLE spectra of ZCIS nanorods. Furthermore, the single-particle Raman spectroscopy, based on the SERS (surface-enhanced Raman scattering) effect, is being elaborated now and already shows promising results.[50] According to the literature, ZCIS NPs with a Cu(In)/Zn ratio of 0.4–0.6 reveal an absorption feature at ~370 nm and a PL peak at ~540–570 nm.[38] The average composition of the sample ZnS : CIS 2 : 1 of 0.5 fits perfectly in this range. Even though the PL and PLE spectra of the sample ZnS : CIS 2 : 1 differ from those of the other three samples (with lower Zn contents), the transformation of the PL spectra is not abrupt. One can see an obvious low-wavelength component (~580 nm) already at a lower Zn content, in samples ZnS : CIS 1 : 1 and ZnS : CIS 3 : 2 (and maybe even ZnS : CIS 1 : 2 if highly zoomed in). Therefore, there is a continuous transition from red to green PL bands with the increasing Zn content. Even though changes of PL spectra of alloyed ZCIS NPs usually occur as a continuous blue shift of a *single* emission band as a whole,[39] the shift accompanied by changes of the spectral line shape similar to those in Fig. 7 was also observed.[38] The position of the PL peaks in ref. 38 is shifted to red, compared to our results (1.05 and 1.35 eV), and the distance between the two PL components is smaller (250 meV), which is probably due to the absence of quantum confinement in the films studied in ref. 37. The gradual transformation of the PL line shape from short- to long-wavelength asymmetry with the increasing Zn content is often observed in other studies on ZCIS NPs; however, it is usually much less pronounced.[47] Obviously, the PL spectra of both ZCIS and CIS have a multi-component structure.[11] The observed change of the PL line shape with a Zn content can be due to enhancement of some recombination channels and/or suppression of others. The broad-band PL emission in CIS and ZCIS NPs is commonly assigned to D-A recombination,[22] but the nature of underlying defects needs a separate thorough study, also at a single nanoparticle level.

Growth process

The size distribution of the samples does not depend on the method in which the educts were brought together (heating-up or hot injection). However, the hot injection method allows for a more precise control of the reaction time and determination of the beginning of the reaction. That is why we used this method for capturing different growth stages of the nanorods, which are described in the following paragraphs.

The first compound, which we find in aliquots taken from the reaction solution after the injection of the sulfur source, is copper thiolate. The X-ray diffraction pattern of this intermediate exactly matches the patterns reported in other studies, reporting the formation of thiolate compounds as

intermediates in the generation of CIS nanocrystals.[4,51] However, in contrast to other studies, in which this pattern is assigned to RS(Cu, In) complexes,[4,51] our EDX measurements do not show the presence of indium (or zinc). $Cu(SC_{12}H_{25})_2$ exhibits narrow reflections corresponding to $0k0$ planes, from which we calculated an average value of 3.56 nm for the 010 spacing of the layered structure. This value matches well with that reported for copper 1-dodecanethiolate.[52] Thus, we conclude that pure copper thiolate is formed in our case, which is most likely due to the high stability of this compound composed of a soft Lewis acid (copper ions) and a soft Lewis base (1-DDT). On the other hand, indium and zinc ions (hard Lewis acids) can be efficiently stabilized by the oleic acid and oleylamine (hard Lewis bases) present in high concentration in the reaction solution, which also promotes the formation of pure copper thiolate. Indium oleate can react at elevated temperatures with oleylamine to form indium hydroxide.[53] Also here, we observe the formation of this compound (reflections marked with blue asterisks in Fig. 10).

First nanoparticles, which are formed during the growth process of ZCIS nanorods, are small (1–3 nm), quasi-spherical copper sulfide particles, which appear about 3.5 min after the injection of the sulfur source. The diameter of these particles increases in the first stage of the reaction, and their size distribution becomes more uniform (see Fig. 10a and b). Because of their small size and, consequently, strong broadening of the reflections in the X-ray diffraction patterns, their crystallographic structure cannot be unambiguously assigned. However, in the sample taken at 5 min 40 s, we can find reflections matching the djurleite structure of copper sulfide (see the red dashed lines in Fig. 10).

The formation of short nanorods can be observed about 8 minutes after the beginning of the reaction (Fig. 11c). At this time, also the composition of the particles changes: the nanocrystals are still copper rich; however, their indium and zinc contents increase (Fig. 12b). Even though the growth process of the nanorods starts with the formation of copper sulfide seeds, we do not detect hybrid nanostructures composed of distinct copper sulfide and ZCIS domains at any stage of the synthesis. This is in agreement with our recent study on the influence of the size of the copper sulfide seeds on the growth process of CIS nanorods, showing that for small seeds copper sulfide is gradually converted to CIS, while hybrid nanocrystals (copper sulfide–CIS) form only from larger seeds.[27]

The nanorods reach their final composition about 10 minutes after the beginning of the reaction. Therefore, the lattice parameters and, consequently, the positions of the reflections in the X-ray diffraction patterns do not change during further growth (Fig. 10). However, the broadening of the reflections and their relative intensity substantially change during further reaction, which is due to changes in the size of the particles and to texture effects. The Rietveld

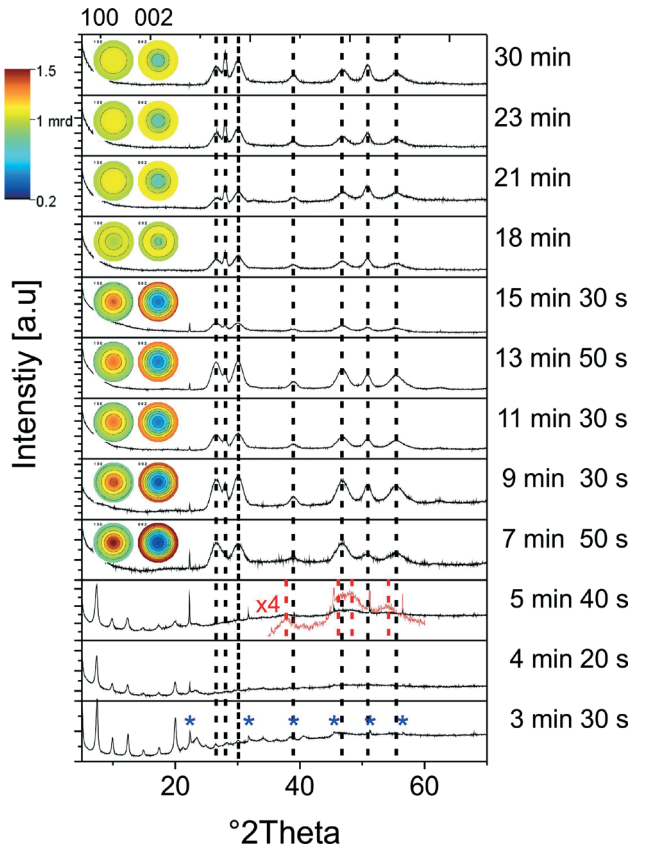

Fig. 10 XRD patterns of aliquots taken at different stages of the growth process of the nanorods; for a better comparison, the positions of the reflections of the ZCIS nanorods are marked by dotted black lines. Reflections stemming from $In(OH)_3$ are marked by blue asterisks. The insets show the pole figures illustrating the texture effects for the 100 and 002 planes. Dotted red lines: djurleite reflections, reference code: 00-023-0959.

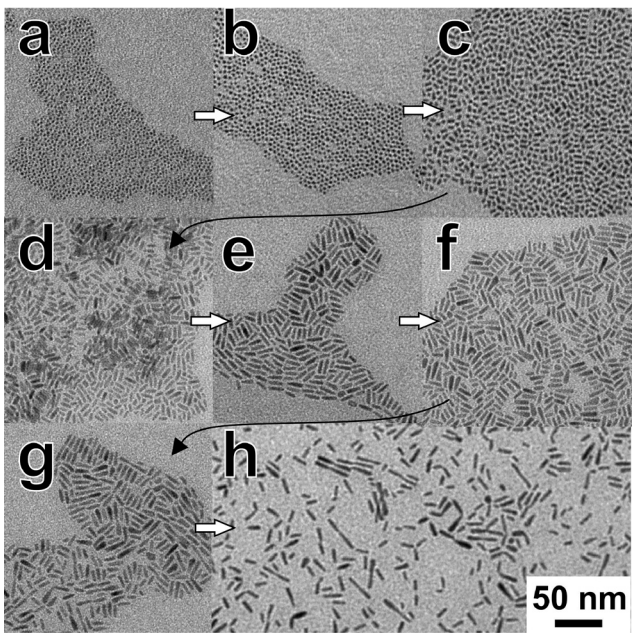

Fig. 11 TEM images of aliquots taken at different stages of the growth process of the nanorods (a: 3 min 30 s, b: 5 min 40 s, c: 7 min 50 s, d: 9 min 30 s, e: 11 min 30 s, f: 13 min 50 s, g: 18 min 10 s, h: 23 min).

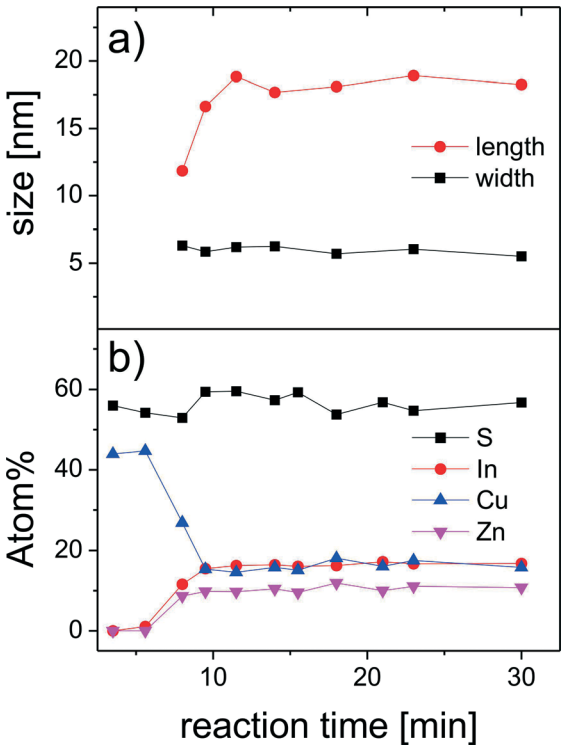

Fig. 12 Temporal evolution of the size of the nanorods during the reaction obtained from the analysis of the XRD data (a). Changes in the composition of the reaction products measured by EDX (b).

analysis of the diffraction patterns reveals that the diameter of the nanorods does not change during the growth process, while their length increases during the first stage of the reaction (Fig. 12a), which can also be seen in the TEM images in Fig. 11. This primary growth ends ~13 minutes after the injection. However, at the later stages of the reaction (20–30 min), we observe a secondary growth process, during which the nanorods start forming dimers (Fig. 11h). Such aggregation does not lead to the formation of longer single-crystalline nanorods; the size of the crystalline domains remains unchanged. The individual nanorods have a strong tendency to be oriented with the long axis parallel to the substrate, as can be seen from the pole figures shown as insets in Fig. 10, indicating a preferential orientation perpendicular to the substrate for the (002) lattice planes, while a large fraction of the (100) lattice planes are parallel to the substrate. The latter results in a low relative intensity of the 002 reflections in the diffraction patterns of the corresponding particles. This tendency changes when the secondary growth and the formation of dimers start. Those aggregated particles are more randomly oriented on the substrate, because of the more irregular shapes, which results in substantially less pronounced texture effects. Thus, the aggregation process can also clearly be detected when analyzing the diffraction patterns.

We attribute this secondary growth to the changes in the stabilization of the particles, caused by the reaction between oleylamine and oleic acid, which takes place at elevated temperatures in the presence of metal cations.[54,55] In the absence of Zn, it leads to the formation of networks of nanorods.[27] Such strong aggregation is not observed here, indicating a more efficient stabilization of ZCIS, compared to pure CIS nanorods.

Conclusions

Alloyed ZCIS nanorods were synthesized with the fraction of Zn incorporated into the CIS lattice controllable in an easy and predictable manner, thus, allowing for the tuning of their optical properties. The growth of the nanorods starts with the formation of copper sulfide particles, which serve as seeds for further generation of ZCIS with an elongated shape. The formation of uniform ZCIS nanorods takes place during heating-up reaction, which opens up the possibility of scaling up this process and producing larger amounts of this material, which is interesting from the point of view of future applications of such ZCIS nanorods.

Acknowledgements

We gratefully acknowledge funding of the EWE Research Group "Thin Film Photovoltaics" by the EWE AG, Oldenburg. Research in Poland was supported by projects DEC-2013/10/E/ST3/00034 from the National Science Center and ORGANOMET no: PBS2/A5/40/2014 from the National Research and Development Center. VD thanks Alexander von Humboldt Foundation for funding.

Notes and references

1 D. Aldakov, A. Lefrançois and P. Reiss, *J. Phys. Chem. C*, 2013, **1**, 3756–3776.
2 J. Kolny-Olesiak and H. Weller, *ACS Appl. Mater. Interfaces*, 2013, **5**, 12221–12237.
3 Y. Zhao and C. Burda, *Energy Environ. Sci.*, 2012, **5**, 5564–5576.
4 H. Zhong, Y. Zhou, M. Ye, Y. He, J. Ye, C. He, C. Yang and Y. Li, *Chem. Mater.*, 2008, **20**, 6434–6443.
5 M. Krunks, O. Bijakina, T. Varema, V. Mikli and E. Mellikov, *Thin Solid Films*, 1999, **338**, 125–130.
6 I. Tsuji, H. Kato, H. Kobayashi and A. Kudo, *J. Phys. Chem. B*, 2005, **2**, 7323–7329.
7 W. Guo, N. Chen, Y. Tu, C. Dong, B. Zhang, C. Hu and J. Chang, *Theranostics*, 2013, **3**, 99–108.
8 K. Yu, P. Ng, J. Ouyang, M. Badruz Zaman, A. Abulrob, T. N. Baral, D. Fetehi, Z. J. Jakubek, D. Kingston, X. Wu, X. Liu, C. Hebert, D. M. Leek and D. M. Whitfield, *ACS Appl. Mater. Interfaces*, 2013, **5**, 2870–2880.
9 X. Tang, W. Cheng, E. S. G. Choo and J. Xue, *Chem. Commun.*, 2011, 5217–5219.
10 Y. Lin, F. Zhang, D. Pan, H. Li and Y. Lu, *J. Mater. Chem.*, 2012, **22**, 8759–8763.
11 W. Zhang and X. Zhong, *Inorg. Chem.*, 2011, **50**, 4065–4072.
12 L. Yi, Y. Liu, N. Yang, Z. Tang, H. Zhao, G. Ma, Z. Su and D. Wang, *Energy Environ. Sci.*, 2013, **6**, 835–840.

13 J. Yang, C. Bao, J. Zhang, T. Yu, H. Huang, Y. Wei, H. Gao, G. Fu, J. Liu and Z. Zou, *Chem. Commun.*, 2013, **49**, 2028–2030.
14 W. Song and H. Yang, *Chem. Mater.*, 2012, **24**, 1961–1967.
15 Y. Zhang, C. Xie, H. Su, J. Liu, S. Pickering, Y. Wang, W. W. Yu, J. Wang, Y. Wang, J. Hahm, N. Dellas, S. E. Mohney and J. Xu, *Nano Lett.*, 2011, **11**, 329–332.
16 B. Chen, H. Zhong, W. Zhang, Z. Tan, Y. Li, C. Yu, T. Zhai, Y. Bando, S. Yang and B. Zou, *Adv. Funct. Mater.*, 2012, **22**, 2081–2088.
17 Z. Tan, Y. Zhang, C. Xie, H. Su, J. Liu, C. Zhang, N. Dellas, S. E. Mohney, Y. Wang, J. Wang and J. Xu, *Adv. Mater.*, 2011, **23**, 3553–3558.
18 J. Feng, M. Sun, F. Yang and X. Yang, *Chem. Commun.*, 2011, **47**, 6422–6424.
19 X. Wang, D. Pan, D. Weng, C. Y. C.-Y. Low, L. Rice, J. Han and Y. Lu, *J. Phys. Chem. C*, 2010, **114**, 13406–13413.
20 D. Pan, D. Weng, X. Wang, Q. Xiao, W. Chen, C. Xu, Z. Yang and Y. Lu, *Chem. Commun.*, 2009, 4221–4223.
21 H. Nakamura, W. Kato, M. Uehara, K. Nose, T. Omata, S. Otsuka-Yao-Matsuo, M. Miyazaki and H. Maeda, *Chem. Mater.*, 2006, **18**, 3330–3335.
22 L. De Trizio, M. Prato, A. Genovese, A. Casu, M. Povia, R. Simonutti, M. J. P. Alcocer, C. D. Andrea, F. Tassone and L. Manna, *Chem. Mater.*, 2012, **24**, 2400–2406.
23 M. Kruszynska, H. Borchert, J. Parisi and J. Kolny-Olesiak, *J. Am. Chem. Soc.*, 2010, **132**, 15976–15986.
24 S. T. Connor, C.-M. Hsu, B. D. Weil, S. Aloni and Y. Cui, *J. Am. Chem. Soc.*, 2009, **131**, 4962–4966.
25 J.-Y. Chang and C.-Y. Cheng, *Chem. Commun.*, 2011, **47**, 9089–9091.
26 J. Kolny-Olesiak, *CrystEngComm*, 2014, **16**, 9381–9390.
27 J. Li, M. Bloemen, J. Parisi and J. Kolny-Olesiak, *ACS Appl. Mater. Interfaces*, 2014, **6**, 20535–20543.
28 N. Popa, *J. Appl. Crystallogr.*, 1998, **31**, 176–180.
29 M. Kruszynska, H. Borchert, A. Bachmatiuk, M. H. Rümmeli, B. Buechner, J. Parisi and J. Kolny-Olesiak, *ACS Nano*, 2012, **6**, 5889–5896.
30 M. Kruszynska, H. Borchert, J. Parisi and J. Kolny-Olesiak, *J. Nanopart. Res.*, 2011, **13**, 5815–5824.
31 M. Kruszynska, J. Parisi and J. Kolny-Olesiak, *Zeitschrift für Naturforsch*, 2014, **69a**, 446–450.
32 D. Pan, L. An, Z. Sun, W. Hou, Y. Yang, Z. Yang and Y. Lu, *J. Am. Chem. Soc.*, 2008, **130**, 5620–5621.
33 S. B. Qadri, J. P. Yang, E. F. Skelton and B. R. Ratna, *Appl. Phys. Lett.*, 1997, **70**, 1020.
34 J. Spanier, R. Robinson, F. Zhang, S.-W. Chan and I. Herman, *Phys. Rev. B: Condens. Matter Mater. Phys.*, 2001, **64**, 245407.
35 J. Rockenberger, L. Tröger, A. L. Rogach, M. Tischer, M. Grundmann, A. Eychmüller and H. Weller, *J. Chem. Phys.*, 1998, **108**, 7807.
36 N. Oehl, P. Michalowski, M. Knipper, J. Kolny-Olesiak, T. Plaggenborg and J. Parisi, *J. Phys. Chem. C*, 2014, **118**, 30238–30243.
37 V. Dzhagan, A. Litvinchuk, M. Valakh, M. Kruszynska, J. Kolny-Olesiak, C. Himcinschi and D. R. T. Zahn, *Phys. status solidi*, 2014, **211**, 195–199.
38 T. Enzenhofer, T. Unold and H. W. Schock, *Phys. status solidi*, 2006, **203**, 2624–2629.
39 W. Chung, H. Jung, C. H. Lee and S. H. Kim, *Opt. Express*, 2012, **20**, 25071–25076.
40 M. P. Lisitsa, M. Y. Valakh and N. K. Konovets, *Phys. status solidi*, 1969, **34**, 269–278.
41 X. Fontané, V. Izquierdo-Roca, E. Saucedo, S. Schorr, V. O. Yukhymchuk, M. Y. Valakh, A. Pérez-Rodríguez and J. R. Morante, *J. Alloys Compd.*, 2012, **539**, 190–194.
42 M. Dimitrievska, A. Fairbrother, X. Fontané, T. Jawhari, V. Izquierdo-Roca, E. Saucedo and A. Pérez-Rodríguez, *Appl. Phys. Lett.*, 2014, **104**, 021901.
43 A. Fairbrother, V. Izquierdo-Roca, X. Fontané, M. Ibáñez, A. Cabot, E. Saucedo and A. Pérez-Rodríguez, *CrystEngComm*, 2014, **16**, 4120.
44 V. M. Dzhagan, M. Y. Valakh, A. G. Milekhin, N. A. Yeryukov, D. R. T. Zahn, E. Cassette, T. Pons and B. Dubertret, *J. Phys. Chem. C*, 2013, **117**, 18225–18233.
45 J. I. Pankove, *Optical Processes in Semiconductors*, Courier Corporation, 2012.
46 M. Sun, D. Zhu, W. Ji, P. Jing, X. Wang, W. Xiang and J. Zhao, *ACS Appl. Mater. Interfaces*, 2013, **5**, 12681–12688.
47 J. Zhang and R. Xie, *Chem. Mater.*, 2011, **23**, 3357–3361.
48 T. Takahashi, A. Kudo, S. Kuwabata, A. Ishikawa, H. Ishihara, Y. Tsuboi and T. Torimoto, *J. Phys. Chem. C*, 2013, **117**, 2511–2520.
49 V. K. Komarala, C. Xie, Y. Wang, J. Xu and M. Xiao, *J. Appl. Phys.*, 2012, **111**, 124314.
50 E. Sheremet, A. G. Milekhin, R. D. Rodriguez, T. Weiss, M. Nesterov, E. E. Rodyakina, O. D. Gordan, L. L. Sveshnikova, T. A. Duda, V. A. Gridchin, V. M. Dzhagan, M. Hietschold and D. R. T. Zahn, *Phys. Chem. Chem. Phys.*, 2015, DOI: 10.1039/C4CP05087H.
51 J. Chang and E. Waclawik, *CrystEngComm*, 2013, **15**, 5612–5619.
52 Y.-B. Chen, L. Chen and L.-M. Wu, *Chem. – Eur. J.*, 2008, **14**, 11069–11075.
53 E. Selishcheva, J. Parisi and J. Kolny-Olesiak, *J. Nanopart. Res.*, 2012, **14**, 711.
54 X. Jin, M. Kruszynska, J. Parisi and J. Kolny-Olesiak, *Nano Res.*, 2011, **4**, 824–835.
55 K. Yu, X. Liu, Q. Y. Chen, H. Yang, M. Yang, X. Wang, X. Wang, H. Cao, D. M. Whitfield, C. Hu and Y. Tao, *Angew. Chem., Int. Ed.*, 2014, **53**, 6898–6904.